



OPEN

SUBJECT AREAS:
SPINTRONICS
MAGNETIC DEVICESReceived
28 April 2014Accepted
22 July 2014Published
13 August 2014Correspondence and
requests for materials
should be addressed to
O.K. (olga.kazakova@
npl.co.uk)

Anisotropic Magnetoresistance State Space of Permalloy Nanowires with Domain Wall Pinning Geometry

Héctor Corte-León¹, Vahid Nabaei^{2,3}, Alessandra Manzin², Jonathan Fletcher¹, Patryk Krzysteczko⁴, Hans W. Schumacher⁴ & Olga Kazakova¹¹National Physical Laboratory, Hampton Road, Teddington, TW11 0LW, UK, ²Istituto Nazionale di Ricerca Metrologica (INRIM), Torino, I-10135, Italy, ³Dipartimento Energia, Politecnico di Torino, Torino, I-10129, Italy, ⁴Physikalisch-Technische Bundesanstalt, Braunschweig, D-38116, Germany.

The domain wall-related change in the anisotropic magnetoresistance in L-shaped permalloy nanowires is measured as a function of the magnitude and orientation of the applied magnetic field. The magnetoresistance curves, compiled into so-called domain wall magnetoresistance state space maps, are used to identify highly reproducible transitions between domain states. Magnetic force microscopy and micromagnetic modelling are correlated with the transport measurements of the devices in order to identify different magnetization states. Analysis allows to determine the optimal working parameters for specific devices, such as the minimal field required to switch magnetization or the most appropriate angle for maximal separation of the pinning/depinning fields. Moreover, the complete state space maps can be used to predict evolution of nanodevices in magnetic field without a need of additional electrical measurements and for repayable initialization of magnetic sensors into a well-specified state.

The ability to create and manipulate Domain Walls (DWs) in ferromagnetic nanostructures introduces important prospects for applications in computation logic¹, magnetic storage², as well as for the development of functional elements in novel magnetic sensors^{3,4}. Since the DW displacement is influenced more strongly by the external field than the magnetization rotation, a higher sensitivity of DW-based devices to low signals is expected than in conventional field sensors. Particularly interesting is the possibility of employing DW-based devices for the detection^{3,5,6} and manipulation^{7–10} of magnetic nanoparticles, which are widely used for tagging molecules or cells^{11–13}.

For all the mentioned applications, it is essential that DWs are nucleated and manipulated in a highly controllable way. The success of these technologies largely relies on absolute understanding of DW properties as well as the ability to reproducibly create the same type of DWs in given physical conditions and fully control their dynamics^{9,14,15}. In soft magnetic materials, the accurate and reproducible control of DW position is typically related to the presence of geometrical constrictions, which act as pinning sites for DW formation. A common oversight, however, is that a precise process of pinning and depinning of a DW in the magnetic nanostructure requires exactly the same starting conditions at each time the experiment is conducted.

In this paper, magnetoresistance (MR) measurements are used to characterize the DW behavior in L-shaped Permalloy (Py) nanowires, which were previously proposed for nanoparticle detection^{3,6} as well as magnetic logic applications¹⁶. The geometry of the device allows the formation of a stable DW, which then propagates along one of the device arms by application of external magnetic fields. Because of the anisotropic magnetoresistance (AMR) effect, which manifests in a dependence of the electrical conductivity on the local orientation of the current flow and magnetization direction, resistance changes can be correlated with changes in the magnetization state of the structure. By measuring the resistance variations, it is possible to detect a DW and measure its interaction with additional magnetic fields, for example the one generated by a nanoparticle placed near the corner of the device^{3,6}.

A complete state space map for a 150-nm wide device has been measured using the AMR effect. Different magnetization states have been identified as a function of the applied field magnitude and orientation as well as previous history of the device. The boundaries between different states, which are related to sharp resistance jumps, correspond to changes in the magnetization configuration. While the majority of such boundaries demonstrate regular and reproducible transitions between the main states, which are clearly more suitable for sensing

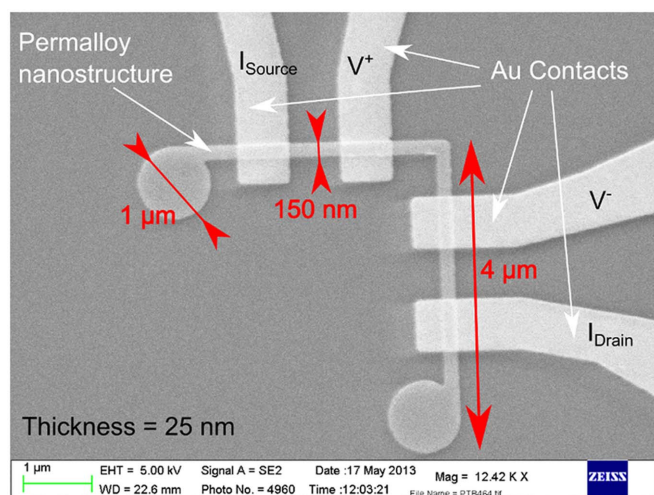


Figure 1 | SEM image of the 150-nm wide L-shaped Py device with gold electrodes.

applications, some of the boundaries are characterized by a stochastic behavior and irregularity of the switching fields. Using the state space map it is possible to identify DW pinning and depinning fields depending on the initial state of the device and predict the evolution of the magnetic state under the application of external magnetic field. The latter property allows avoiding conditions with highly stochastic transitions, while identifying the best ones for sensing applications.

Experimental results have been accompanied by combined micro-magnetic - magnetotransport modelling, which shows a good agreement with measured AMR signals and is used to identify different magnetization states.

Results

An SEM image of a typical L-shaped nanodevice with a schematic of the electrical contacts is shown in Fig. 1 (see Methods for more information).

Remanent magnetic states. Stable magnetic states at zero field have been imaged using a Magnetic Force Microscopy (MFM) technique (Fig. 2). To create these states, a positive field of 17 mT is applied along the direction indicated by the white arrows in Fig. 2. The observed magnetization configurations are in agreement with the

results obtained on similar devices using Magnetic Kerr Effect Microscopy^{16,17}.

Figure 2a shows a DW pinned at the corner of the device with the magnetization of the arms in a head-to-head configuration. This configuration is ascribed as state $[-1, -1]$ referring to the magnetization orientation in the two arms, which is pointing towards the corner in respect to the (x, y) axes (Fig. 2c, inset). Figure 2b displays a state with no DW, in a head-to-tail configuration of the arms, with some inhomogeneity at the corner, overall reflecting a gradual spatial change of the magnetization from one arm to another. This state is named $[1, -1]$. Figure 2c shows a DW in a tail-to-tail configuration of the arms, or state $[1, 1]$. Finally, Fig. 2d depicts a state $[-1, 1]$ with no DW at the corner. The magnetization of the MFM tip does not change through the experiment, allowing proper comparison of all four possible stable states.

Magnetoresistance measurements. We present two types of AMR experiments accompanied by micromagnetic and magnetotransport modeling, which analyze the magnetization states and DW dynamics in the studied nanodevices. *In the first type of experiment* (an angular mapping of MR curves), typical MR hysteresis loops^{17,18} were measured for different angular orientations β of the applied field, *i.e.* $0^\circ < \beta < 90^\circ$ and $90^\circ < \beta < 180^\circ$ where β is the angle between the applied field and the x -arm (Fig. 3 insets). The objective of this experiment is to identify conditions for generating all of stable states. *In the second type of experiment* (state space map), one of the four main domain configurations (Fig. 2) was preset initially. Then the device resistance was measured, while the magnetic field was ramped up at a certain angular orientation. The aim of this experiment is to test all combinations of initial magnetization states and orientations of the applied field in order to build a complete state space map of the device, where both the magnitude and orientation of the field change in small steps. Such state space maps can be used to predict the evolution of the device in a varying magnetic field without the need for additional transport measurements.

Angular mapping of MR curves. In this experiment, the magnetic field is ramped up and down for a fixed angle β (see Fig. 3 insets), while the electrical resistance is measured across the corner^{17,18}. It is important to note that the geometry of the device implies two-fold symmetry of the experimental results making field orientations separated by 180° identical. Due to this geometry, two different

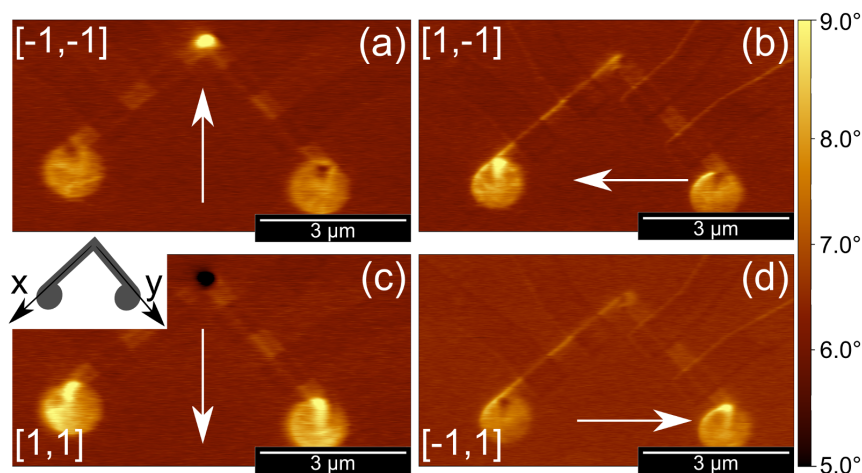


Figure 2 | MFM images of the device after applying a magnetic field of +17 mT in the directions indicated by the white arrows. The images show four possible stable states at zero field. Assuming a constant magnetization along the nanowires and using the (x, y) coordinates, these states can be named as: a) $[-1, -1]$ with a DW at the corner, b) $[1, -1]$ with no DW, c) $[1, 1]$ with a DW at the corner, d) $[-1, 1]$ with no DW. Inset in (c) shows the Cartesian axes (x, y) .

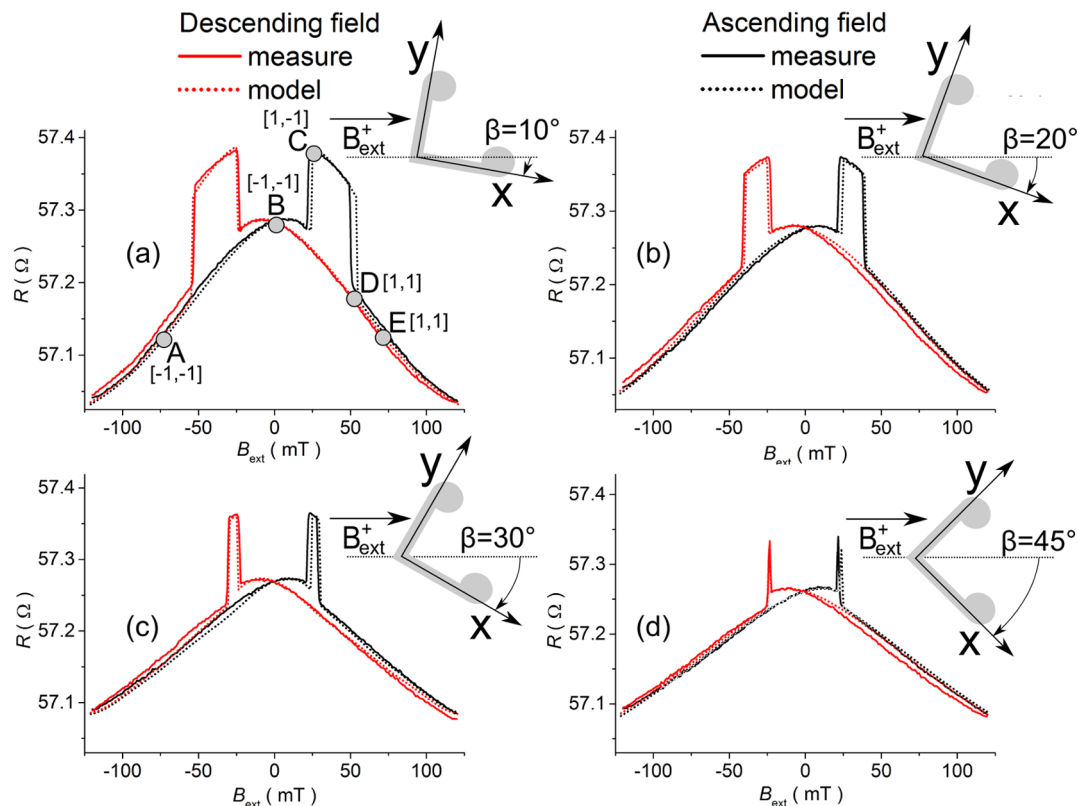


Figure 3 | Measured and simulated AMR curves for $\beta = 10^\circ$ a), $\beta = 20^\circ$ b), $\beta = 30^\circ$ c) and $\beta = 45^\circ$ d). The black line represents the sweeping of the magnetic field from negative to positive values, while the red line shows the descending field branch. Insets show schematic orientation of the device with respect to the magnetic field.

types of reversal mechanisms were observed in an AMR hysteresis loop as a function of device orientation.

Angles $0^\circ < \beta < 90^\circ$. MR measurements were performed for $0^\circ < \beta < 90^\circ$ in 0.9° steps with the magnetic field changing from -120 to 120 mT in 0.6 mT steps. Figure 3 shows the experimental and modeling results obtained for four representative angles. The micromagnetic modeling was performed using typical magnetic parameters for Py, *i.e.* setting the magnetization saturation and the exchange constant at 860 kA/m and 13 pJ/m, respectively, and

excluding magnetocrystalline anisotropy term. In agreement with the thickness dependence of Py electrical properties¹⁹, the magneto-transport simulations have been performed by fixing σ_0 (the electrical conductivity when the material is saturated due to an external field orthogonal to the current flow) to 4 MS/m (*i.e.* the resistivity to 25 $\mu\Omega$ cm). The modeled magnetoresistance curves reported in the following have been obtained by setting the AMR ratio at 1%, after a preliminary parametric analysis oriented to the determination of the value that leads to the best agreement with the experimental results. This value belongs to the parameter range

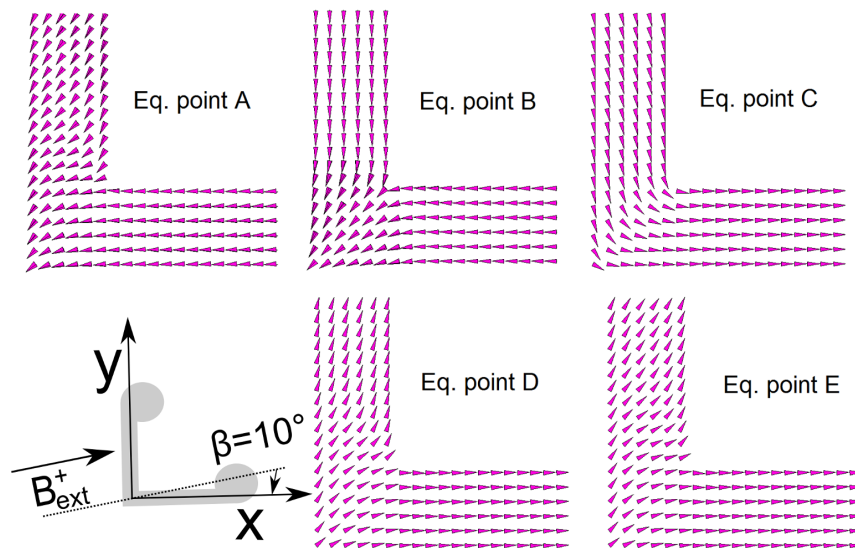


Figure 4 | Computed magnetization spatial configurations at the device corner for the equilibrium points indicated in Fig. 3a at $\beta = 10^\circ$.

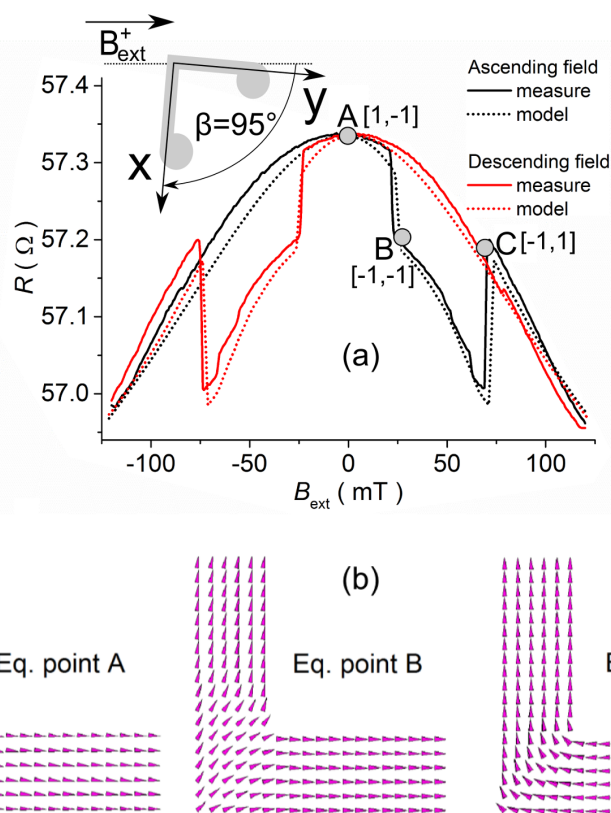


Figure 5 | (a) Measured and simulated AMR curves at $\beta = 95^\circ$. The black line represents the sweeping of the magnetic field from negative to positive values, while the red line is associated with the descending field branch. (b) Computed magnetization spatial configurations at the device corner for the equilibrium points indicated in a).

typical for Py, which varies from 1 to 5%, depending on the amount of nickel in the alloy²⁰. The magnetic field in the simulations was changed in 1.6 mT steps. For these experimental and modeling parameters, a very good agreement is reached for both the shape of the AMR curves and the electrical resistance values. This confirms that in Py nanodevices the MR properties are dominated by the AMR effect.

Using the magnetic domain configuration obtained by micromagnetic modeling, it is possible to interpret AMR curves in terms of DW pinning/depinning processes. In the AMR curves presented in Fig. 3a, a number of equilibrium points have been labeled together with the corresponding magnetization states. The detailed magnetic configuration of the device at these points is shown in Fig. 4. Following the black line in Fig. 3a, starting from a high negative field value at point A (*i.e.* the maximum applied field is -120 mT, while point A is ~ -75 mT), the horizontal arm is uniformly magnetized along the x-negative axis, while the magnetization in the other arm is aligned at a certain angle with respect to the field direction. This state corresponds to a low resistance value. When moving towards remanence (point B at 0 mT), the magnetization of the vertical arm becomes parallel to the y-axis, hence increasing the resistance²¹. The state $[-1, -1]$ corresponds to a DW pinned at the corner, where magnetizations of both arms are aligned along x and y axes. Point C (in the range 17.0–22.5 mT (± 1 mT) depending on the exact angle) indicates depinning of the DW from the corner and the transition to state $[1, -1]$. Switching of the horizontal arm is favored at small angles $\beta < 45^\circ$, since in this case the component of the magnetic field along the x-axis is higher. When the magnetic field increases further, in point D (in the range 52–55 mT (± 1 mT)) the vertical component of the magnetic field is high enough to allow the second switching event and the consequent pinning of another DW. This corresponds to a state $[1, 1]$. Between equilibrium points C and D the resistance

reaches the highest value because of the AMR effect (magnetization and current density vectors are nearly parallel). After point D, the resistance gradually decreases with the field, due to the rotation of the magnetization towards the external field direction. As the field increases, the magnetization tends to deviate from the easy direction, starting from the arm aligned along the y-axis, since it experiences the highest transversal magnetic field (point E). A symmetrical behavior is observed when the external field is swept from high positive to high negative fields (red curve, in Fig. 3a) for both simulated and experimental data.

For the other angles shown in Fig. 3, the behavior is qualitatively the same as presented in Fig. 3a. However, when the angle β increases from 0° to 45° , the range of fields between equilibrium points C and D (*i.e.* the high resistance range characterized by the absence of the DW) gets progressively narrower. For example, for $\beta = 0^\circ$ the difference between points C and D is maximal, ~ 108 mT (*i.e.* point C is at ~ 21 mT and D is at ~ 129 mT), while at $\beta = 45^\circ$ this difference is nearly zero, *i.e.* both C and D transitions occur almost at the same field of ~ 21 mT. This demonstrates that the state without a DW becomes energetically favorable only in a very narrow range of magnetic fields for this geometrical configuration. A similar sequence of pinning/depinning events and their angular dependence were observed by others¹⁶ as well as in our Magneto Optical measurements on identical Py devices, where switching of the individual arm's magnetization can be directly measured¹⁷.

Angles $90^\circ < \beta < 180^\circ$. The same type of experiment was repeated for angular orientations $90^\circ < \beta < 180^\circ$, where a significant change in the switching pattern was observed. An example of the AMR curves modeled and measured at $\beta = 95^\circ$ and relevant computed magnetic domain configurations are shown in Fig. 5. Using these results, the different shapes of AMR curves can be interpreted as a change in the

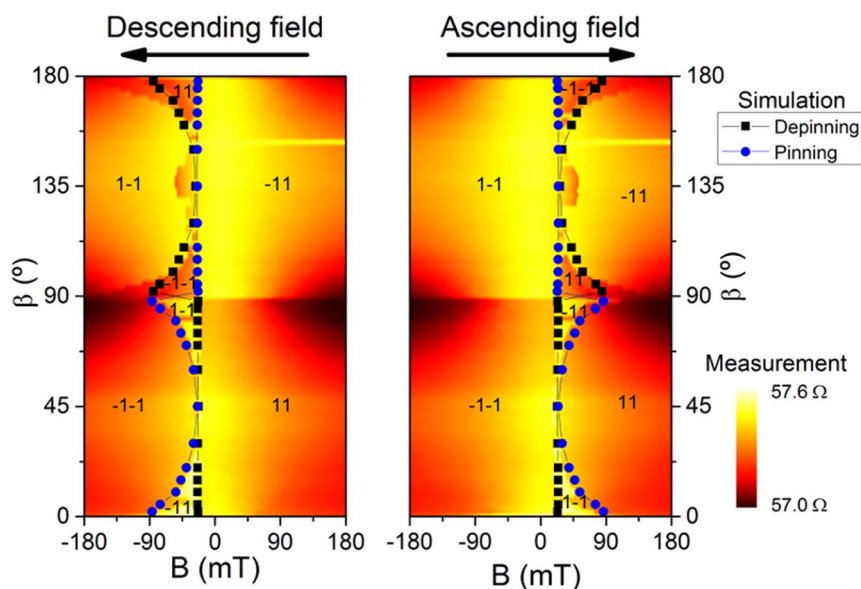


Figure 6 | Averaged 2D maps of the AMR dependence on the angular orientation β and the magnitude of the external magnetic field. The field sweeps from a high positive to a high negative value (left) and vice versa (right). Magnetization states are identified in respect to x-y axis, see Fig. 3a. The calculated DW pinning/depinning fields are identified by square and dot symbols, as specified in the legend.

order of pinning/depinning events, similar to the experiments described before. For angles $90^\circ < \beta < 180^\circ$ (and $270^\circ < \beta < 360^\circ$), a high magnetic field (120 mT in this case) leads to a magnetization state without a DW at the corner. As the magnetic field increases, first pinning of a DW indicated by a decrease in the resistance is observed at point B (in the range 21–33 mT (± 1 mT)), which is followed by a depinning event at point C seen as the associated resistance increment (in the range 35–141 mT (± 1 mT)), see Fig. 5.

Complete angular mapping. Using the setup described above, 10 consecutive MR loops have been measured for each orientation at $0^\circ < \beta < 180^\circ$ with a step of 1.8° . The averaged hysteresis loops resulting from these measurements are shown in Fig. 6 where the color scale represents the resistance of the device. To clarify the results, the sweeping of the magnetic field from negative to positive values is plotted in the right-side panel, while the sweeping from positive to negative is reported in the left-side one. The DW pinning and depinning processes are observed as sharp borders between the areas of different shading. In the same figure, the different magnetization states as well as the pinning/depinning fields extracted from simulations have been marked.

The maps in Fig. 6 demonstrate an angular dependence of the reversal mechanism in the L-shaped Py nanostructure and agree well with reported results for non-interacting Py nanowires of similar width and thickness^{22–24}. For $0^\circ < \beta < 90^\circ$ (Fig. 6 lower part of the maps), the first resistance jump (DW depinning) occurs at 17–21 mT (± 1 mT) and is nearly independent of β (i.e. variation is below 5 mT). On the contrary, the DW pinning field associated with the second resistance jump is strongly influenced by β and varies smoothly in the range 23–130 mT (± 1 mT). This angular dependence is related to the component of the applied field along the direction of each arm. The pinning/depinning event corresponds to the switching of an individual arm. For one arm, the switching field is a function of $\cos(\beta)$, while for the other one, it is a function of $\cos(\pi/2 - \beta)$. These dependencies are swapped at 45° and 135° . This consideration explains why the first resistance jump is only weakly influenced by the angular orientation. However, a larger influence is expected when the nanowire width is reduced, due to the increase in the arm coercivity and, consequently, in the field leading to

magnetization reversal. The lowest field values are reached at $\beta \approx 45^\circ$. In this case, the two critical fields are of approximately the same value, $\sim 21 \pm 1$ mT. This is due to the fact that the magnetization reversal takes place nearly simultaneously in both arms due to the device symmetry, as also demonstrated in Fig. 3d. A similar situation is observed for $90^\circ < \beta < 180^\circ$ where, however the characteristic behavior of pinning/depinning fields is swapped (Fig. 6 upper part of the maps). In this case, the DW pinning field has a small angular dependence, changing in the range 21–33 mT (± 1 mT), while the DW depinning field is characterized by a strong angular dependence, changing in the range 35–141 mT (± 1 mT).

The averaging procedure used here reduces the fine effects related to the internal structure of the DW. These effects appear stochastically during measurements and are experimentally observed as pinning/depinning events taking place at different fields^{25–29}. It also minimizes the effects of fabrication and film growth defects, however some fine features seen in Fig. 6 still can be attributed to such device/material defects and inhomogeneities.

The angular dependence of DW pinning/depinning fields has also been studied using magnetotransport simulations, which show a very good agreement with experimental data for both angular ranges (see dots in Fig. 6 and Ref. 18). While the modelling results describe the main experimental tendency very well, there are still some additional experimental features not reflected in the modelling (see e.g. in Fig. 6 transitions at $\sim 10^\circ$ and 80° , where pinning events occur at a lower than expected value). Since the measurements have been averaged, these differences can be attributed to defects in the structure (i.e. edge roughness or internal defects). However, some minor features, for example low-field transitions around $\beta = 135^\circ$, are not observed in the simulations. These features could be attributed to development of a quasi-single domain state in low fields. An evidence for this can be seen as an additional domain sub-structure occupying a small part of the device corner in the remanent state after application of the field at $\beta = 135^\circ$ (see, e.g. Fig. 2 b and d). As the field evolves, these substructures propagate through the device causing the additional steps of the magnetoresistance.

We further separate the influence of defects and the stochastic behavior. Fig. 7a shows individual (i.e. not averaged) space state maps for two different devices of the same width $w = 150$ nm.

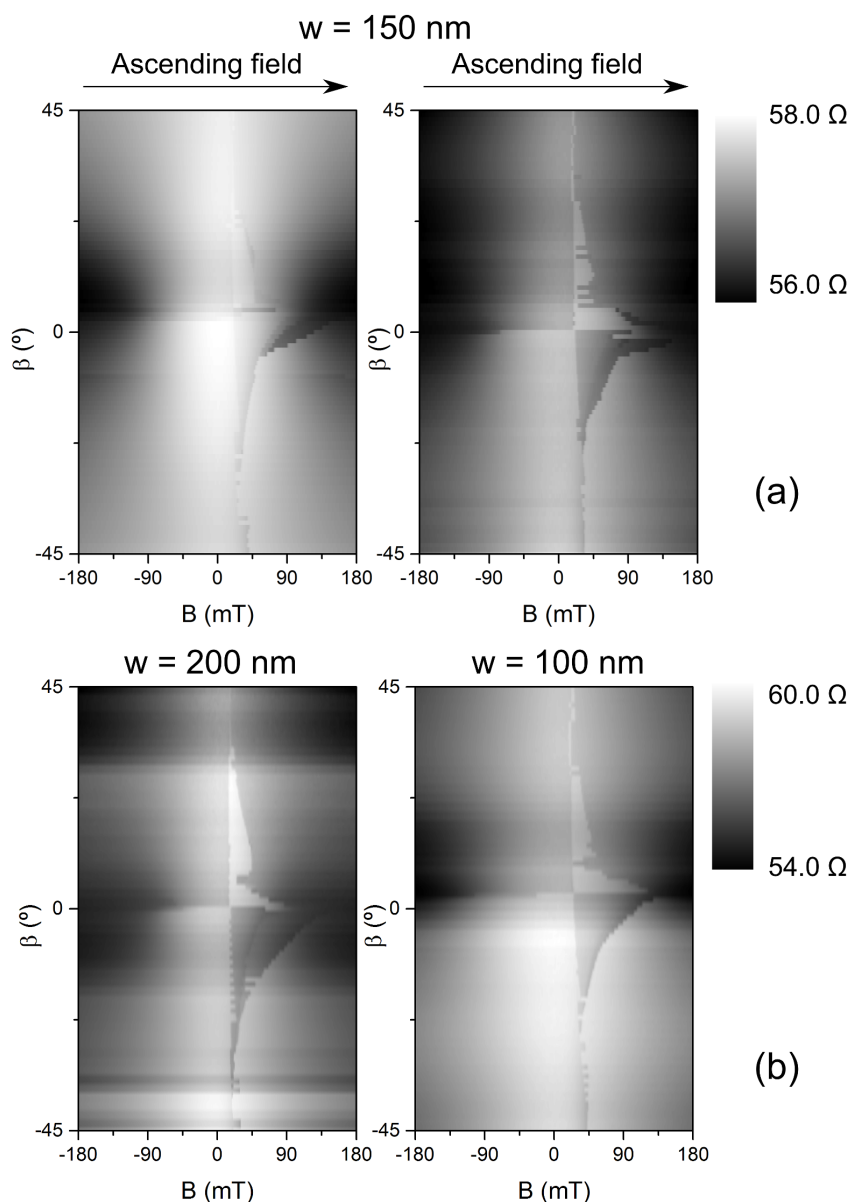


Figure 7 | Single (*i.e.* not averaged) space state maps for different devices, showing the effect of the stochastic behaviour between individual measurements and the width dependence of the pinning/depinning fields: a) two different devices of 150-nm width; b) devices with the width of 200 nm (left) and 100 nm (right).

The figure demonstrates that minor individual pinning/depinning events might change stochastically between individual measurement runs. However, overall ‘shape’ of the space state and reliable working points remain the same for both devices (for example, in all cases $\beta \sim 45^\circ$ and $B \sim 60$ mT corresponds to a state [1,1]).

To compare the effect of width variation, Fig. 7b shows space state maps of two different devices with $w = 100$ nm (right) and 200 nm (left). From analyses of Fig. 7, we conclude that the qualitative behaviour remains the same in the studied width range. Additionally, we observe reduction in the absolute values of pinning/depinning fields as well as in the difference between them as the device width increases. Thus, for the presented width range, the stochastic behavior is not significantly affected by variations in the domain wall structure.

The results shown in Fig. 6 and 7 allow to predict the behavior of the device upon exposure to the either large or small external magnetic fields, corresponding to major or minor hysteresis loops (*i.e.* switch of both or only one arm, respectively) as reported by Donolato

et al.^{3,6}. In more complex situations, where both the magnitude and orientation of the magnetic field change at the same time, a state-space map similar to the one presented in the next section is needed.

State space map. The experiments described above allow understanding of the behavior of the device and the study of its evolution under different experimental conditions but not when both the magnitude and orientation of the magnetic field are changed at the same time. Thus, the second type of experiment is performed to create a state space map linking the changes in resistance of the device with its magnetization state. This experiment allows to predict the DW evolution under a time-dependent external magnetic field that changes both magnitude and orientation, bearing in mind a significantly higher velocity of DW motion in comparison with the typical ramping time of the magnetic field.

A complete state space map is shown in Fig. 8a. The main difference with the previous results (Fig. 6) is that the device was initially set into one of the four stable and well-defined states, by applying first

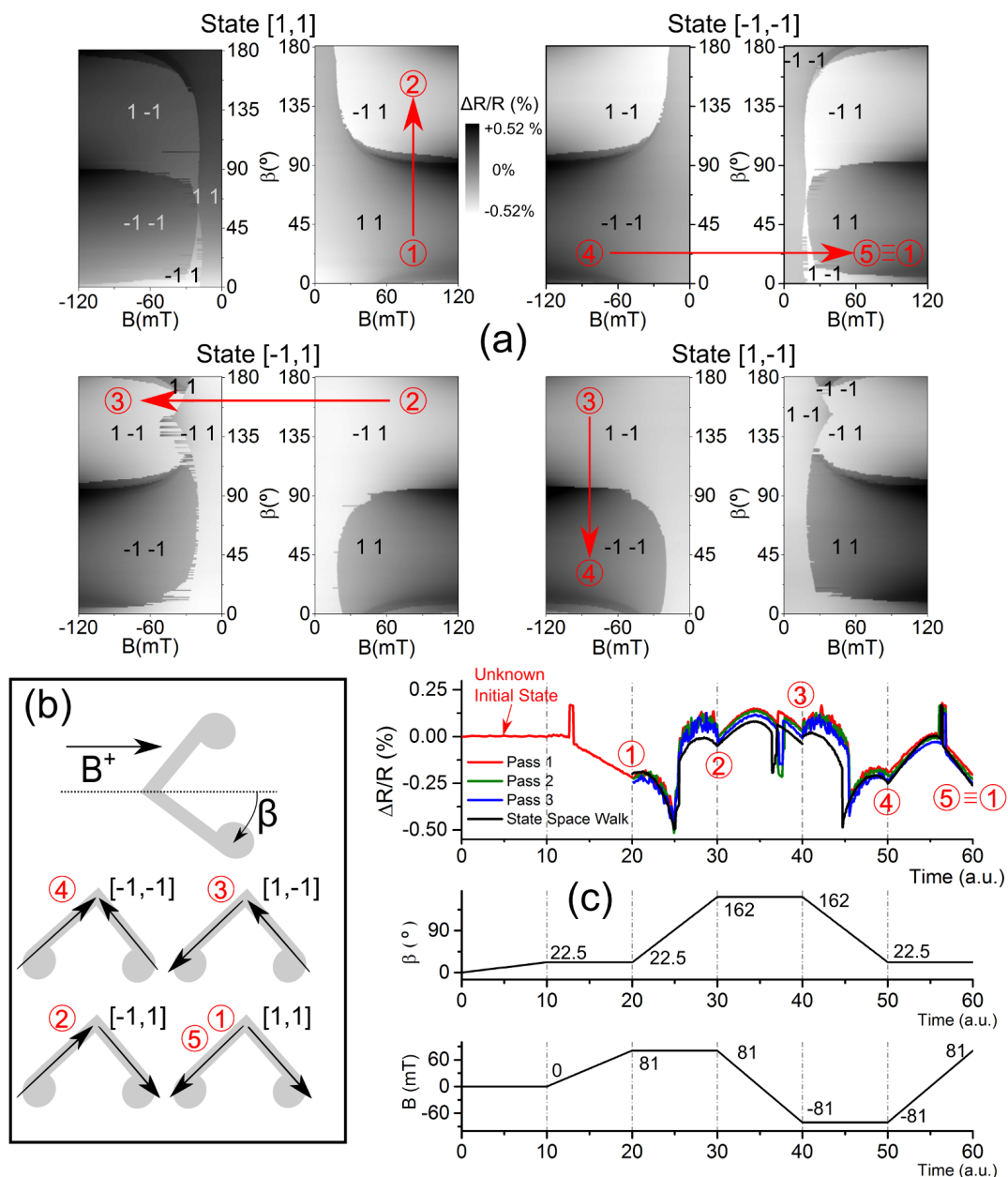


Figure 8 | (a) Complete state space for a 150-nm wide Py device. The initial state at zero magnetic field is shown on top of each panel. The red numbers and arrows indicate the path followed by an individual AMR measurement to test the validity of the state space. The greyscale represents the change of the AMR signal. (b) Schematic of the device orientation and state configuration with respect to x-y axes. (c) Top: (black) data extracted from (a) represents the evolution of the resistance, when the device follows the path 1-5. (Other colors) experimentally measured data when the device follows the path 1-5. Colors represent different experimental runs. Middle and bottom: Schematic change of the field orientation and magnitude, respectively.

a large external magnetic field (120 mT) at either 45° or 135° (as previously confirmed by MFM in Fig. 2 and AMR in Fig. 6). The state of the device is then changed by applying another field at a fixed angle $0^\circ < \beta < 180^\circ$, while recording the device resistance. This procedure is repeated using all the four identified stable states as initial configurations and for all orientations of the second field. Data from Fig. 6 is used to identify the exact conditions (*i.e.* magnitude and orientation of the external field) needed for generating each of the stable states. For example, to create a tail-to-tail state at zero field (state $[1,1]$), the device should be placed at an angle $40^\circ < \beta < 50^\circ$ and magnetic field $B \geq 60$ mT (under these conditions state $[1,1]$ is always observed experimentally, see Fig. 6). Alternatively, to create a head-to-head configuration (state $[-1,-1]$), the device should be put at an angle $40^\circ < \beta < 50^\circ$ and magnetic field $B \leq -60$ mT. To

create head-to-tail and tail-to-head configurations (*i.e.* $[-1,1]$ and $[1,-1]$, respectively) the same procedure can be used, using $140^\circ < \beta < 150^\circ$ and $B \geq 60$ mT or $B \leq -60$ mT, respectively.

Figure 8a also demonstrates how different initial magnetization states may evolve into other states (see Fig. 8b for angular orientations and state configurations). Using the same principle as before, two magnetization configurations are considered identical if the transition between them occurs without a sharp change in the resistance (*i.e.* no pinning/depinning of DW is involved in the process) and without saturating the magnetization by the external magnetic field. No new stable states were observed during the measurement of the map. Thus, the state space can be considered complete, in the sense that the device always evolves only into one of the already known states.


Table 1 | The orientation and magnitude of the applied field for the arbitrary path selected in Fig. 8a and extracted in Fig. 8c (black line)

Path	Initial β (degrees)	Final β (degrees)	Initial Field (mT)	Final Field (mT)	State transition
	($\pm 0.9^\circ$)	($\pm 0.9^\circ$)	(± 0.6 mT)	(± 0.6 mT)	
1–2	22.5	162.0	81	81	$[1, 1] \rightarrow [-1, 1]$
2–3	162.0	162.0	81	–81	$[-1, 1] \rightarrow [1, 1] \rightarrow [1, -1]$
3–4	162.0	22.5	–81	–81	$[1, -1] \rightarrow [-1, -1]$
4–5	22.5	22.5	–81	81	$[-1, -1] \rightarrow [1, -1] \rightarrow [1, 1]$

Whereas the majority of boundaries in Fig. 8a are sharp, a few of them exhibit significantly stochastic behaviour (see *e.g.* bottom left panel in Fig. 8a showing stochastic transitions from state $[-1, 1]$), indicating that either the transition is unstable, *i.e.* might occur at two different fields^{25,27}, or there are stochastic pinning/depinning events taking place²⁶. An example of such behavior is shown for the $[-1, 1]$ to $[1, -1]$ transition at $\beta = 135^\circ$ and $B < 0$, where for some of the runs switching occurs at different fields (Fig. 8a, bottom left panel).

The state space map shown in Fig. 8a allows to reliably predict the device evolution under a changing external magnetic field and define a procedure for the initialization of future DW-based sensors, *i.e.* putting them into a well-defined magnetization configuration. This last property is extremely important, since for sensing applications, the proximity of a small magnetic object (*e.g.* a magnetic nanobead) will result in a shift of the DW pinning/depinning fields³ and some transitions might be more favorable than others. The state space map allows to select the optimal transition parameters to measure this effect.

In order to illustrate how to initialize the device into a particular state and use the map to track this state, an arbitrary path (*i.e.* evolution of an applied magnetic field) has been selected to test the predicted transitions between different states. Red numbers in Fig. 8a and data in Table 1 indicate the chosen path in the state space. The resistance changes of the device along this path have been extracted from the existing map and presented in Fig. 8c as a black line which connects points 1 to 5, corresponding to evolution of the magnitude and orientation of the magnetic field as depicted in Fig. 8c (middle and bottom) and Table 1.

The red line in Fig. 8c (top) represents real magnetotransport measurements for the same combination of the fields. Despite the unknown initial state, as soon as the external conditions, *i.e.* magnetic field amplitude and orientation, approach the ones corresponding to point 1 (Fig. 8c, middle and bottom), the device evolves into a $[1, 1]$ state. A small difference in the resistance between extracted data and measurements is likely to be caused by thermal effects. From point 1 to point 2, the magnetic field remains constant, while the angle increases from 22.5° to 162° . When the orientation is close to 90° there is a change in the state of the device, from $[1, 1]$ to $[-1, 1]$, as predicted by the map (Fig. 8a). From point 2 to point 3, the orientation remains constant and the field changes from $+81$ mT to -81 mT. The state of the device changes from $[-1, 1]$ to $[1, -1]$. Here, the measured profile agrees with the extracted one, but the transition occurs at a slightly different field. On the state space map, the transition 2–3 corresponds to the crossing of the border with significantly high density of stochastic switching and a strong angular dependence. At the transition 3–4, the device is rotated again and the state changes from $[1, -1]$ to $[-1, -1]$. Finally, the transition 4–5 corresponds to sweeping of the magnetic field from -81 mT to $+81$ mT without a change of the field orientation and results in the change of the device state from $[-1, -1]$ to $[1, 1]$. The second sweep of the magnetic field occurs in an area with a low probability of stochastic transitions and small angular dependence. This results in a better agreement between experimental and extracted paths for the profile 4–5 in comparison to the profile 2–3

and indicates that such transition is potentially better suitable for detection of small shifts due to external magnetic fields (*i.e.* due to presence of a nanoparticle). Point 5 is identical to point 1, both in terms of the external conditions and the internal state of the device ($[1, 1]$). Thus, the cycle is completed. To test reproducibility of the states, a number of consecutive runs have been performed immediately afterwards (Fig. 8c, blue and green curves). All the curves demonstrate a very good match between individual runs and agreement with the predicted jumps in the resistance due to DW propagation. It is noteworthy that in all the runs the resistance measurements are less stable when the magnetic field changes its orientation rather than value. The effect is due to the physical rotation of the sample stage and the associated mechanical vibrations.

Discussion

We have performed detailed magnetotransport measurements in L-shaped Py nanostructures allowing for precise correlation of their magnetization state and changes in resistance. Such devices have promising applications, *e.g.* as MR sensors for magnetic bead detection. The direct comparison is possible due to a simple magnetic state of the device characterized by absence/presence of a DW, which can be pinned/depinned at the corner of the nanostructure.

By varying the orientation of the external magnetic field, we identified the angular dependence of the DW pinning and depinning fields. Due to symmetry of the nanostructure, two different types of reversal mechanisms were observed as a function of the device orientation. For angles $0^\circ < \beta < 90^\circ$ (and $180^\circ < \beta < 270^\circ$), the change of the resistance is characterized by the depinning of the DW from the device corner, followed by nucleation of another DW in the disk and pinning at the corner. An opposite behavior (pinning followed by depinning) is found for $90^\circ < \beta < 180^\circ$ (and $270^\circ < \beta < 360^\circ$). We show that whichever switching event (pinning or depinning) occurring first it has a small angular dependence, while the second switching event is characterized by a significantly stronger angular dependence.

The angular dependence of DW pinning and depinning fields has also been studied using magnetotransport simulations, which show a very good agreement with experimental data. Using modelling and MFM experiments, it was possible to identify all remanent magnetization states and correlate them to the transitions observed in magnetotransport measurements.

By varying the field magnitude and orientation, we plot 2D maps of the device MR (state space maps), which allow for a clear identification of four main magnetization configurations characterised by the presence/absence of the DW. The boundaries between different states, characterised by sharp resistance jumps, correspond to abrupt changes in the domain configuration. Whereas majority of transitions between the states occurs through a sharp boundary demonstrating regular and reproducible transitions between the main states, some of them are characterised by an increased probability of stochastic switching. The first type of transitions is clearly the most suitable for sensing applications. Using the state space maps, it is possible to identify DW pinning and depinning fields. Such state space maps are extremely useful for determination of working parameters, such as the minimum field needed to switch both arms at



different device orientations, or the most appropriate angle for maximal separation of the pinning and depinning fields. Thus, space maps help to optimize the best conditions for sensing applications.

A complete state space map also allows for prediction of the DW evolution under an external magnetic field which varies both in magnitude and orientation without need of repeating MR or MFM measurements. These predictions were tested experimentally against real magnetotransport measurements with the results showing a very good experimental agreement. These findings are important for the reliable initialization of arrays of DW sensors into a well-specified sensing state.

Methods

The nanostructures were fabricated from a continuous polycrystalline Py film sputtered on top of a Si/SiO_x substrate. The Py layer is 25 nm thick and covered by a 2 nm Pt cap to prevent oxidation. Standard e-beam lithography in combination with Ar-ion etching has been used to pattern the Py films into L-shaped nanowires with a width of 100, 150 and 200 nm (Fig. 1), following the design proposed in Ref. 3. The structure includes two arms of 4 μm length at 90° to each other with discs of 1 μm diameter at each end. In a second lithography step, Au contact leads for electrical transport measurements were fabricated via thermal evaporation of Ti (10 nm) and Au (60 nm). Prior to deposition of the electrodes, the Py surface was cleaned with low energy Ar ions.

Electrical experimental setup. AMR measurements through the corner were performed at room temperature using the 4-point resistance configuration as shown in Fig. 1. The injected AC current is fixed to 10 μA r.m.s. at 172 Hz. The AC signal is generated using a lock-in amplifier, with a resistor placed before the I_{source} connector to fix the current through the device. The current is drained to ground through the I_{drain} connector in series with a 50-Ω resistor. Voltage through the corner is measured using the contacts marked as V+ and V− in Fig. 1 and amplified with a 100 gain factor. A voltage divider is used to scale the original lock-in signal and subtract it from the amplified voltage from the device, allowing to measure only the resistance change. Using this differential method, it is possible to measure only the change of the resistance induced by AMR effect after subtracting the background.

The magnetic field is applied using a dipole electromagnet. The maximum value of the applied field is 180 mT, and the field changes in steps of 0.6 mT at a rate of 40 ms per step.

The sample holder is attached to a step motor, which allows to change orientation of the device in respect to the magnetic field. The motor is mounted 25 cm away from the sample and drives the sample holder through a non-magnetic shaft. The rotation of the motor is fixed with a step of 0.9°, allowing for 360° rotation in the substrate plane. The reference for the rotation of the device is set, defining an angle β between one of the device's arms and the external magnetic field (see the inset in Fig. 3a). Following the initial optical positioning of the device, alignment of the system is done by measuring MR hysteresis loops and defining β = 0° (90°) when the loop type is abruptly changed as shown in Fig. 6.

Modelling. To complement electrical transport measurements and MFM imaging, the experimental results have been supported by MR modelling of the AMR effect. The adopted modelling approach, combining a micromagnetic solver³⁰ with a transport model, enables interpretation of the experimental MR curves, infers DW dynamics and identifies the external field conditions leading to DW pinning and depinning.

The AMR phenomenon is simulated reproducing the non-uniform spatial distributions of current density vector and electrical conductivity associated with equilibrium magnetization configurations, separating time scales for electronic transport and magnetic ordering, and neglecting galvanomagnetic effects. The magnetization spatial distribution at each applied field value is calculated using a micromagnetic solver designed to efficiently solve the Landau-Lifshitz-Gilbert (LLG) equation in micron-sized magnetic samples³⁰. Specifically, the magnetic nanostructure is meshed into hexahedra, within each of which the magnetization vector **M** is assumed to be uniform and locally computed by integrating the LLG equation:

$$\frac{\partial \mathbf{M}}{\partial t} = -\frac{\gamma}{1+\alpha^2} \mathbf{M} \times \left[\mathbf{H}_{eff} + \frac{\alpha}{M_S} (\mathbf{M} \times \mathbf{H}_{eff}) \right] \quad (1)$$

where γ is the absolute value of gyromagnetic ratio, α is the damping coefficient, M_S is the saturation magnetization and **H**_{eff} is the effective field, which is the sum of the magnetostatic, exchange, anisotropy and external fields. To preserve the magnetization amplitude, the LLG equation is time-integrated by using a norm-conserving formalism based on Cayley transform and a second-order Heun scheme³¹. To accurately calculate the effective field avoiding fictitious anisotropy effects in correspondence of curved boundaries, the exchange field is derived from a finite difference algorithm able to handle unstructured meshes, thus not imposing restrictions on the mesh element shape³².

After computing the magnetization configuration at each equilibrium point, the associated distribution of the current density vector **J** is obtained by considering

steady-state conditions and by solving the following transport equation with finite element method and linear basis functions

$$\nabla \cdot [\sigma(\mathbf{r}) \nabla \phi(\mathbf{r})] \quad (2)$$

where φ is the electric scalar potential (**E** = -∇φ, **E** being the electric field) and σ(**r**) is the local electrical conductivity that is expressed as a function of the angle θ between vectors **M** and **J**, i.e.

$$\sigma(\mathbf{r}) = \frac{\sigma_0}{1 + \kappa \cos^2 \theta(\mathbf{r})} \quad (3)$$

where σ₀ is the electrical conductivity when the material is saturated due to an external magnetic field applied orthogonally to the current flow and κ is the AMR ratio^{18,33}. This expression simply describes the dependence of the electrical resistance on the angle between the current direction and the magnetization orientation. Specifically, the local electrical conductivity is minimal when current density and magnetization vectors are parallel or anti-parallel, while it is maximal when they are orthogonally oriented.

The problem formulation is completed by ad-hoc boundary conditions. Specifically, the current flow in respect to current contacts is imposed through an integral constraint (current-driven problem) and the voltage contacts are modeled as highly conductive regions while at insulating boundaries the normal component of the current density vector is imposed to zero. Finally, non-linear equation (2) is iteratively solved until reaching convergence of both conductivity and current density distributions.

- Allwood, D. A. *et al.* Magnetic domain-wall logic. *Science* **309**, 1688–92 (2005).
- Thomas, L., Hughes, B., Rettner, C. & Parkin, S. S. P. Racetrack Memory: A high-performance, low-cost, non-volatile memory based on magnetic domain walls. *2011 Int. Electron Devices Meet.* 24.2.1–24.2.4 (2011). doi:10.1109/IEDM.2011.6131603.
- Donolato, M. *et al.* Nanosized corners for trapping and detecting magnetic nanoparticles. *Nanotechnology* **20**, 385501 (2009).
- Kunz, A., Reiff, S. C., Priem, J. D. & Rentsch, E. W. Controlling individual domain walls in ferromagnetic nanowires for memory and sensor applications. *2010 Int. Conf. Electromagn. Adv. Appl.* 248–251 (2010). doi:10.1109/ICEAA.2010.5653609.
- Vavassori, P. *et al.* Domain wall displacement in Py square ring for single nanometric magnetic bead detection. *Appl. Phys. Lett.* **93**, 203502 (2008).
- Donolato, M. *et al.* Detection of a single synthetic antiferromagnetic nanoparticle with an AMR nanostructure: Comparison between simulations and experiments. *J. Phys. Conf. Ser.* **200**, 122001 (2010).
- Donolato, M. *et al.* Magnetic domain wall conduits for single cell applications. *Lab Chip* **11**, 2976–83 (2011).
- Bryan, M. T. *et al.* The effect of trapping superparamagnetic beads on domain wall motion. *Appl. Phys. Lett.* **96**, 192503 (2010).
- Chen, A., Byvank, T., Vieira, G. B., Sooryakumar, R. & Substrates, A. Magnetic Microstructures for Control of Brownian Motion and Microparticle Transport. **49**, 300–308 (2013).
- Rapopot, E. & Beach, G. S. D. Dynamics of superparamagnetic microbead transport along magnetic nanotracks by magnetic domain walls. *Appl. Phys. Lett.* **100**, 082401 (2012).
- Sun, X., Ho, D., Lacroix, L., Xiao, J. Q. & Sun, S. Magnetic Nanoparticles for Magnetoresistance-Based Biodetection. **11**, 46–53 (2012).
- Furlani, E. P. Magnetic Biotransport: Analysis and Applications. *Materials (Basel)* **3**, 2412–2446 (2010).
- Skomski, R. Nanomagnetism. *J. Phys. Condens. Matter* **15**, R841–R896 (2003).
- Kläui, M. *et al.* Controlled and Reproducible Domain Wall Displacement by Current Pulses Injected into Ferromagnetic Ring Structures. *Phys. Rev. Lett.* **94**, 106601 (2005).
- Rodríguez, L. A. *et al.* Optimized cobalt nanowires for domain wall manipulation imaged by in situ Lorentz microscopy. *Appl. Phys. Lett.* **102**, 022418 (2013).
- Allwood, D. A. *et al.* Shifted hysteresis loops from magnetic nanowires. *Appl. Phys. Lett.* **81**, 4005 (2002).
- Beguivín, A. *et al.* Simultaneous magnetoresistance and magneto-optical measurements of domain wall properties in nanodevices. *J. Appl. Phys.* **115**, 17C718 (2014).
- Manzin, A. *et al.* Modeling of anisotropic magnetoresistance properties of permalloy nanostructures. *IEEE Trans. Magn.* **50** (2014).
- Bogart, L. K. & Atkinson, D. Domain wall anisotropic magnetoresistance in planar nanowires. *Appl. Phys. Lett.* **94**, 042511 (2009).
- McGuire, T. R. & Potter, R. I. Anisotropic Magnetoresistance in Ferromagnetic 3d Alloys. *IEEE Trans. Magn.* **MAG-11**, 1018–1038 (1975).
- Manago, T., Kanazawa, K. & Kera, T. Magneto-resistance of NiFe nanowire with zigzag shape. *J. Magn. Magn. Mater.* **321**, 2327–2330 (2009).
- Oliveira, A., Rezende, S. & Azevedo, A. Magnetization reversal in permalloy ferromagnetic nanowires investigated with magnetoresistance measurements. *Phys. Rev. B* **78**, 024423 (2008).



23. Moon, K., Lee, J., Jung, M., Shin, K. & Choe, S. Incoherent Domain Configuration Along Wire Width in Permalloy Nanowires. *IEEE Trans. Magn.* **45**, 2485–2487 (2009).
24. Wegrowe, J.-E., Kelly, D., Franck, A., Gilbert, S. & Ansermet, J.-P. Magnetoresistance of Ferromagnetic Nanowires. *Phys. Rev. Lett.* **82**, 3681–3684 (1999).
25. Hayashi, M. *et al.* Dependence of Current and Field Driven Depinning of Domain Walls on Their Structure and Chirality in Permalloy Nanowires. *Phys. Rev. Lett.* **97**, 207205 (2006).
26. Muñoz, M. & Prieto, J. L. Suppression of the intrinsic stochastic pinning of domain walls in magnetic nanostripes. *Nat. Commun.* **2**, 562 (2011).
27. Akerman, J., Muñoz, M., Maicas, M. & Prieto, J. L. Stochastic nature of the domain wall depinning in permalloy magnetic nanowires. *Phys. Rev. B* **82**, 064426 (2010).
28. Hayashi, M., Thomas, L., Rettner, C., Moriya, R. & Parkin, S. S. P. Direct observation of the coherent precession of magnetic domain walls propagating along permalloy nanowires. *Nat. Phys.* **3**, 21–25 (2006).
29. Holmes, S. N. *et al.* Magnetic vortex stability in Ni80Fe20 split rings. *J. Appl. Phys.* **113**, 044508 (2013).
30. Manzin, A. & Bottauscio, O. A Micromagnetic Solver for Large-Scale Patterned Media Based on Non-Structured Meshing. *IEEE Trans. Magn.* **48**, 2789–2792 (2012).
31. Manzin, A. & Bottauscio, O. Connections between numerical behavior and physical parameters in the micromagnetic computation of static hysteresis loops. *J. Appl. Phys.* **108**, 093917 (2010).
32. Bottauscio, O. & Manzin, A. Spatial Reconstruction of Exchange Field Interactions With a Finite Difference Scheme Based on Unstructured Meshes. *IEEE Trans. Magn.* **48**, 3250–3253 (2012).
33. Bordignon, G. *et al.* Analysis of Magnetoresistance in Arrays of Connected Nano-Rings. *IEEE Trans. Magn.* **43**, 2881–2883 (2007).

Acknowledgments

This work has been cofunded by EMRP and the EMRP participating countries under Project EMRP IND08 (MetMags) and Project EXL04 (SpinCal). We are very grateful to Anthony Beguivin, Russell Cowburn and James Wells for useful discussions.

Author contributions

O.K. and H.W.S. designed the research, P.K. fabricated the devices, H.C.L. and J.F. developed the measurement setup, H.C.L. performed the experiments, H.C.L. and O.K. analysed the data, A.M. and V.N. developed the numerical model and performed simulations. All authors discussed the results. H.C.L., A.M. and O.K. participated in writing the manuscript. All authors reviewed and commented on the manuscript.

Additional information

Competing financial interests: The authors declare no competing financial interests.

How to cite this article: Corte-León, H. *et al.* Anisotropic Magnetoresistance State Space of Permalloy Nanowires with Domain Wall Pinning Geometry. *Sci. Rep.* **4**, 6045; DOI:10.1038/srep06045 (2014).



This work is licensed under a Creative Commons Attribution-NonCommercial-ShareAlike 4.0 International License. The images or other third party material in this article are included in the article's Creative Commons license, unless indicated otherwise in the credit line; if the material is not included under the Creative Commons license, users will need to obtain permission from the license holder in order to reproduce the material. To view a copy of this license, visit <http://creativecommons.org/licenses/by-nc-sa/4.0/>